RSC Advances

PAPER

View Article Online
View Journal | View Issue

Check for updates

Cite this: *RSC Adv.*, 2025, **15**, 42299

Synthesis, characterization and biological studies of pyrazole-linked Schiff bases and their copper(II) complexes as potential therapeutics

Pratima Kumari,[a] Aman Kumar,[a] Ramesh Kataria, *[b] Navin Kumar Kaushik,[c] Mukhtar Ahmed,[a] Azaj Ansari,[a] Ekta,[a] Mettle Brahma,[d] Mulaka Maruthi,[d] Yangala Sudheer Babu,[d] Bijender Singh[e] and Vinod Kumar *[a]

The novel pyrazole-linked Schiff base-derived Cu(II) complexes were prepared, characterized, and evaluated for their biological potential. Single-crystal X-ray diffraction, UV-visible, FT-IR, NMR, EPR spectroscopy, mass spectrometry, and SEM-EDX techniques have been utilized for establishing the chemical structures of the compounds. The results of the single-crystal X-ray diffraction study of complex **4c** disclosed that the prepared copper(II) complexes possess a square planar geometry. Antimalarial screening against *P. falciparum* revealed that the ligand **3d** and copper complexes **4a–d** are more effective, with percentage suppression ranging from 90% to 100%, as determined by the RBC haemolysis assay. Compound **3d** exhibited the highest selectivity index (SI = 18.38), followed by **3e** (SI = 9.48) and **4d** (SI = 6.02). Furthermore, molecular docking simulations were performed on newly prepared ligands and their copper(II) complexes, which support their potential as effective antimalarial agents. An anticancer evaluation study revealed that compound **4b** exhibited remarkable anticancer efficacy with the highest selectivity (SI = 13.48) towards A549 cells, outperforming the reference drugs Cisplatin, Carboplatin, and Dexamethasone. It was observed that complexation with copper ions results in increased selectivity for A549 cells and decreased cytotoxicity towards Vero cells. Moreover, compound **4e** displayed the highest antibacterial potential with an MIC value of 0.02 mg mL^{-1} against *B. subtilis*.

Received 14th August 2025
Accepted 17th October 2025

DOI: 10.1039/d5ra06008g

rsc.li/rsc-advances

Open Access Article. Published on 03 November 2025. Downloaded on 2/11/2026 12:55:24 AM.
This article is licensed under a Creative Commons Attribution-NonCommercial 3.0 Unported Licence.

1. Introduction

The discovery of Cisplatin and Auranofin was a harbinger in the field of metal-based drugs and continues to encourage chemists to investigate metal complexes for potential applications in the field of medicine.[1] Furthermore, metal-based medications can pass through the membrane of microbes and adhere to the genetic materials of such harmful microbes (RNA/DNA).[2] The potential benefits of investigating transition metal complexes lead to the search for safe and efficient therapeutics for various pathogenic disorders.

Among the transition metals, copper(II) ion-based complexes have recently attracted considerable attention in the domain of inorganic synthesis because of some crucial features like borderline Lewis acid behaviour, stereochemical variation, efficiency to vary its oxidation state, and relatively low toxicity to the human body.[3] The revival is partially due to copper's inherent presence in numerous natural biological processes, which regulate copper levels and metabolize it significantly.[4] It is a key component of metalloenzymes that plays a significant role in the process of iron homeostasis, superoxide disproportionation, and production of melanin, catecholamine and neuropeptide.[5] Utilization of copper complexes to treat medical issues has long been a practice, and assessment of the structural properties of such complexes for therapeutic use has made substantial progress[6] (Fig. 1).

In agreement with prior investigations on copper(II) complexes, these complexes can decrease the microvascular supply, tumour volume, and vascular accessibility of several cancer strains.[7a] The copper complexes trigger cancerous cell death either by inducing controlled cell death, which affects only malignant cells and spares healthy cells, or by producing reactive oxygen species under oxidative stress, which damages the genetic material of cancerous cells.[7b,c] These complexes with planar aromatic rings usually attach to DNA and RNA *via* an intercalating mechanism.[7d,e] Since copper complexes are known to be promising bioactive agents, it was decided to investigate their biological potential.

[a]*Department of Chemistry, School of Basic Sciences, Central University of Haryana, Mahendergarh-123031, Haryana, India. E-mail: vinodkumar@cuh.ac.in*

[b]*Department of Chemistry, Panjab University, Chandigarh-160014, India. E-mail: rkataria@pu.ac.in*

[c]*Amity Institute of Virology and Immunology, Amity University, Noida-201313, Uttar Pradesh, India*

[d]*Department of Biochemistry, School of Interdisciplinary and Applied Sciences, Central University of Haryana, Mahendergarh-123031, Haryana, India*

[e]*Department of Biotechnology, School of Interdisciplinary and Applied Sciences, Central University of Haryana, Mahendergarh-123031, Haryana, India*

© 2025 The Author(s). Published by the Royal Society of Chemistry

Open Access Article. Published on 03 November 2025. Downloaded on 2/11/2026 12:55:24 AM.
This article is licensed under a Creative Commons Attribution-NonCommercial 3.0 Unported Licence.

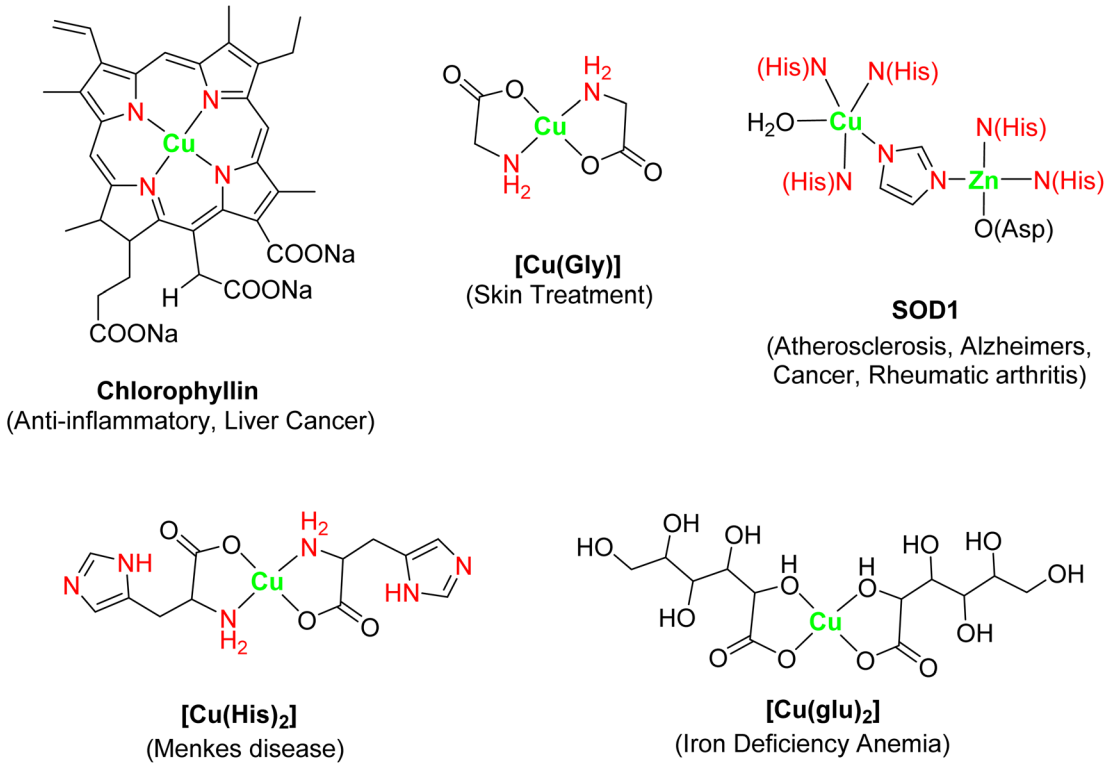

Fig. 1 Some copper(II) complexes used as commercial drugs.

Among the ligand scaffolds, researchers focused primarily on Schiff base ligands due to their well-known structural flexibility, chelating capacity, and numerous therapeutic benefits.[8] It has been well documented that the pyrazole ring, whether in a free or fused state, as a key component of a Schiff's base, displays a broad range of bioactivities, including anticancer, antimalarial, antimicrobial, antitubercular, antileishmanial, anti-inflammatory, and antioxidant properties.[9–17] Numerous pyrazole-containing medications such as antipsychotic CDPPB, powerful anti-inflammatory Mepirizole, Epirizole, Lonazolac, Celecoxib, antiobesity rimonabant, analgesic Difenamizole, antidepressant Fezolamine, an H_2-receptor agonist Betazole, and many more, have been developed and are being used to treat several kinds of disorders[18] (Fig. 2).

In view of the facts mentioned, it was worthwhile to synthesize new copper(II) complexes of pyrazole-linked Schiff base ligands with the expectation of getting potential bioactive agents.

The preparation of 1,3,4-trisubstituted pyrazole-based Schiff's base chelating ligands and their Cu(II) complexes is described here, and their *in vitro* antimalarial, anticancer, and antimicrobial activities were also evaluated. The biological outcomes of Schiff's base ligands and their associated copper(II) complexes were further supported by theoretical investigations.

2. Results and discussion

2.1 Chemistry

Some new pyrazole-linked Schiff's bases and their copper(II) complexes were prepared using a multistep process, as shown in Schemes 1 and 2. To synthesize these new compounds, initially, various hydrazones (**3′a–e**) were prepared according to the literature procedure,[19] which on reaction with Vilsmeier–Haack reagent yielded intermediates, 3-aryl-1-phenyl-1*H*-pyrazole-3-carbaldehydes (**4′a–e**). Further, aldehydes were oxidized using aqueous $KMnO_4$, *tert*-BuOH to yield the corresponding acids[20] **5′a–e**, which on esterification using methanol in the presence of $SOCl_2$ produced **6′a–e** in good yields.[21] Following the reaction conditions as reported,[22] esters were heated with an excess of hydrazine hydrate in ethanol to yield the corresponding acid hydrazides **1a–e**. The structures of **4′a–e** to **1a–e** were confirmed based on their physical and spectral data as given in Table S1 (SI).

In Scheme 2, Schiff base ligands (**3a–e**) were obtained by refluxing acid hydrazides with dehydroacetic acid (DHA) in ethanol. Finally, the complexes **4a–e** were prepared according to literature[23] by adopting a simple procedure that involves the reaction of ligands with copper(II) salt in methanol.

Physical data of compounds **3a–e** and **4a–e** are present in Table S2 (SI). It has been observed from thermogravimetric results that the compounds **4a–e** are stable up to 220 °C. Single crystal XRD spectral investigations verified the square planar structure of the copper(II) complexes and binding sites *via* nitrogen and oxygen atoms of the Schiff's bases with Cu(II) ions in a tridentate mode (Fig. 4).

2.2 Spectral and physical techniques

Numerous analytical examinations were conducted to determine the ligands' binding properties, the complexes' structures

© 2025 The Author(s). Published by the Royal Society of Chemistry

Open Access Article. Published on 03 November 2025. Downloaded on 2/11/2026 12:55:24 AM.
This article is licensed under a Creative Commons Attribution-NonCommercial 3.0 Unported Licence.

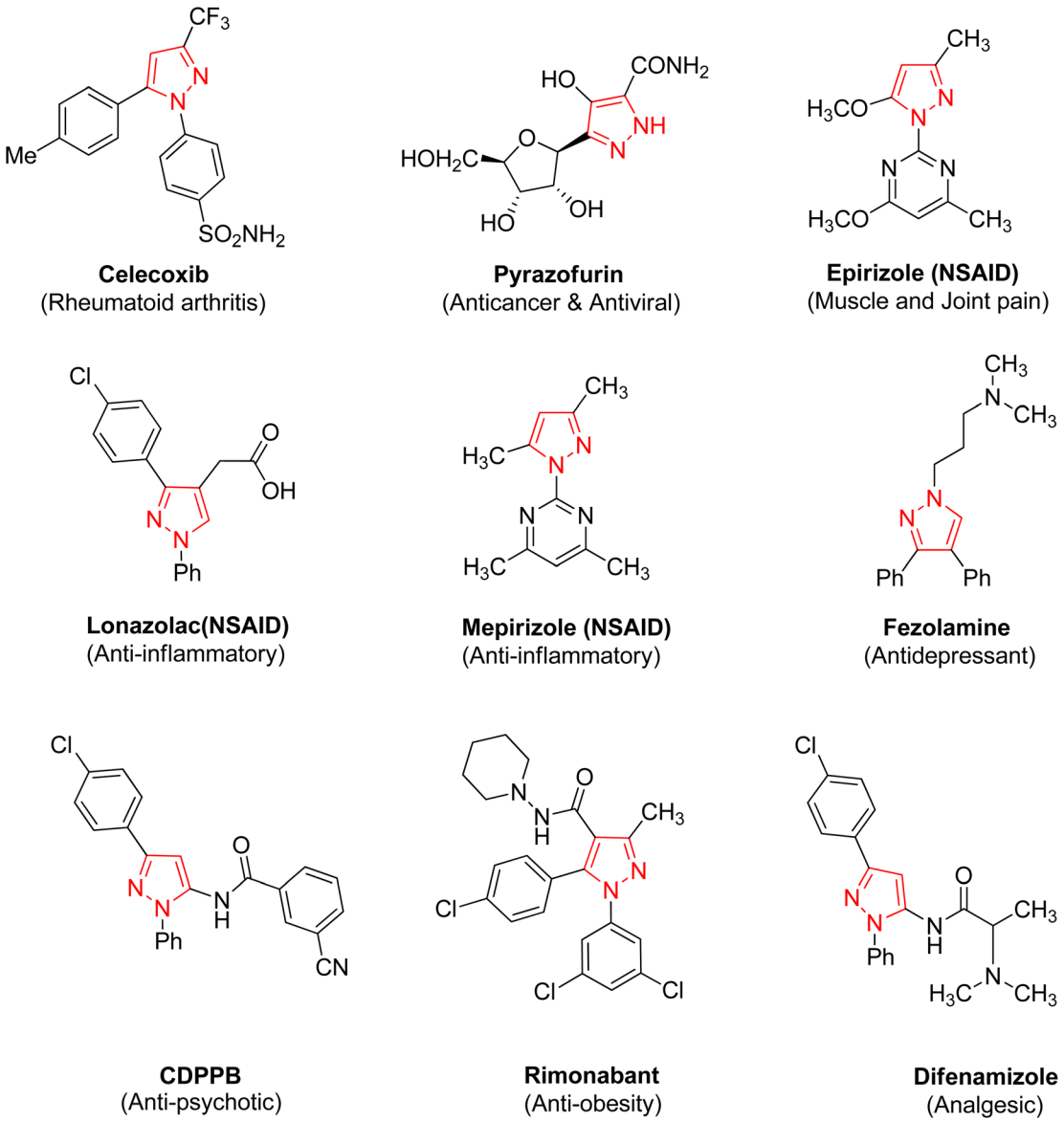

Fig. 2 Some pyrazole-based commercial drugs.

and their purity, morphology, and decomposition, as discussed below. Detailed spectroscopic data of the compounds, **3a–e** and **4a–e** have been given in the SI.

2.2.1 UV-vis spectroscopy. Apart from the single crystal X-ray diffraction results, the complex's stereochemistry is confirmed by analyzing UV-vis spectral data (Fig. 11, SI). The ligands **3a–e** exhibit two absorption bands at 270–282 nm and 343–376 nm as a result of $\pi \rightarrow \pi^*$ transition of azomethine and $n \rightarrow \pi^*$ transition of the Schiff base ligands, respectively, which changed to 262–264 nm and 362–365 nm after complexation, confirming that ligands and metal atoms are chelated.[24a] The presence of two absorption bands at 447–451 nm and 451–559 nm due to the $^2B_{1g} \rightarrow {}^2E_{1g}$ ($\upsilon 1$) and $^2B_{1g} \rightarrow {}^2A_{1g}$ ($\upsilon 2$) transitions, respectively, in the spectra established the square planar environment around Cu(II) ion, which is in close agreement with the value reported in literature.[24b]

2.2.2 FT-IR spectroscopy. The binding sites in the complexes were established by analyzing the FT-IR spectral data by correlating the IR bands of ligands **3a–e** with their corresponding complexes **4a–e**. The C=O group of DHA moiety of Schiff's base ligands holds a band at 1701–1670 cm^{-1}, which is also present in metal complexes in the frequency range of 1702–1677 cm^{-1}, confirmed that this carbonyl is not involved in complexation, while another C=O group of the ligand gives a strong band at 1648–1641 cm^{-1}, which appeared as a shoulder band with a very low intensity at 1640–1660 cm^{-1} due to keto–enol tautomerism with –NH involvement in complexation with metal ions. Keto–enol tautomerisation and linking *via* the oxygen atom of (C–O) enolic group[25] could be observed by the occurrence of the (C–O) enolic absorption band at 1317–1304 cm^{-1} on complex formation. Appearance of new bands due to M–O and M–N stretching vibrations, appeared at 560–

Open Access Article. Published on 03 November 2025. Downloaded on 2/11/2026 12:55:24 AM.
This article is licensed under a Creative Commons Attribution-NonCommercial 3.0 Unported Licence.

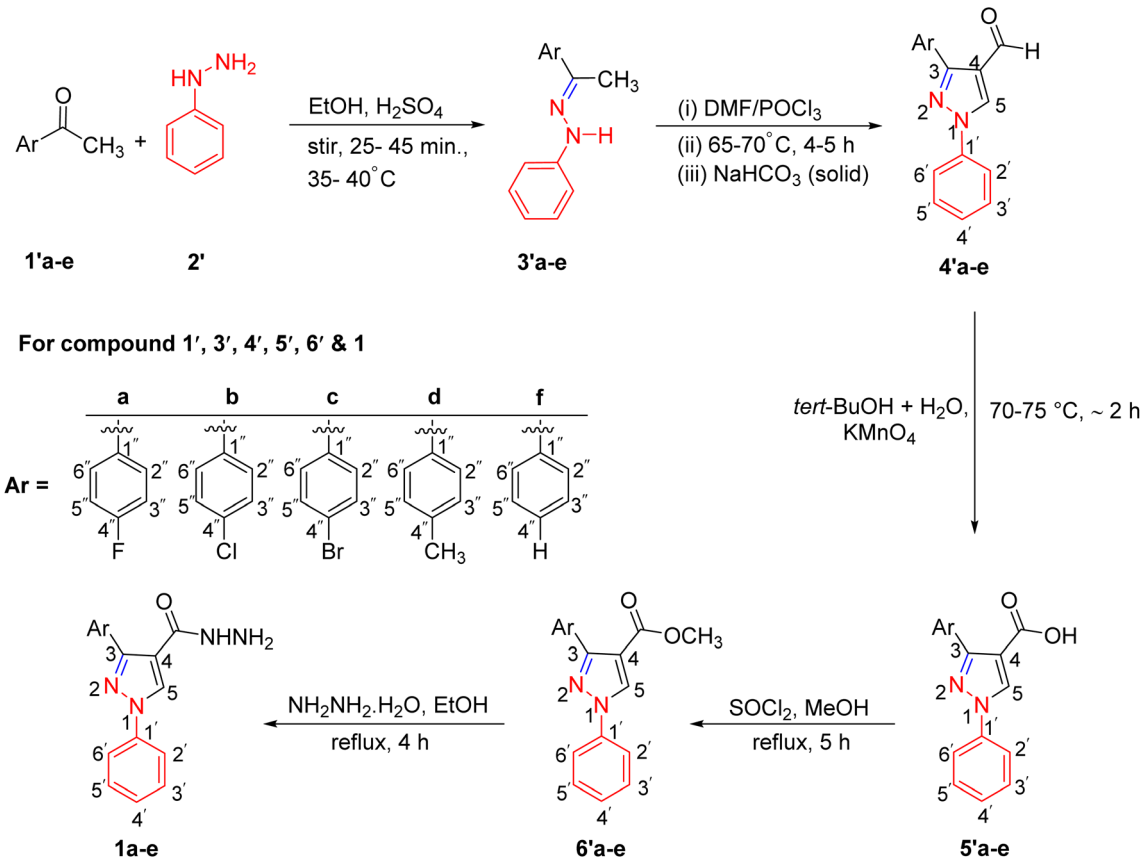

Scheme 1 Synthesis of various intermediates for achieving new ligands.

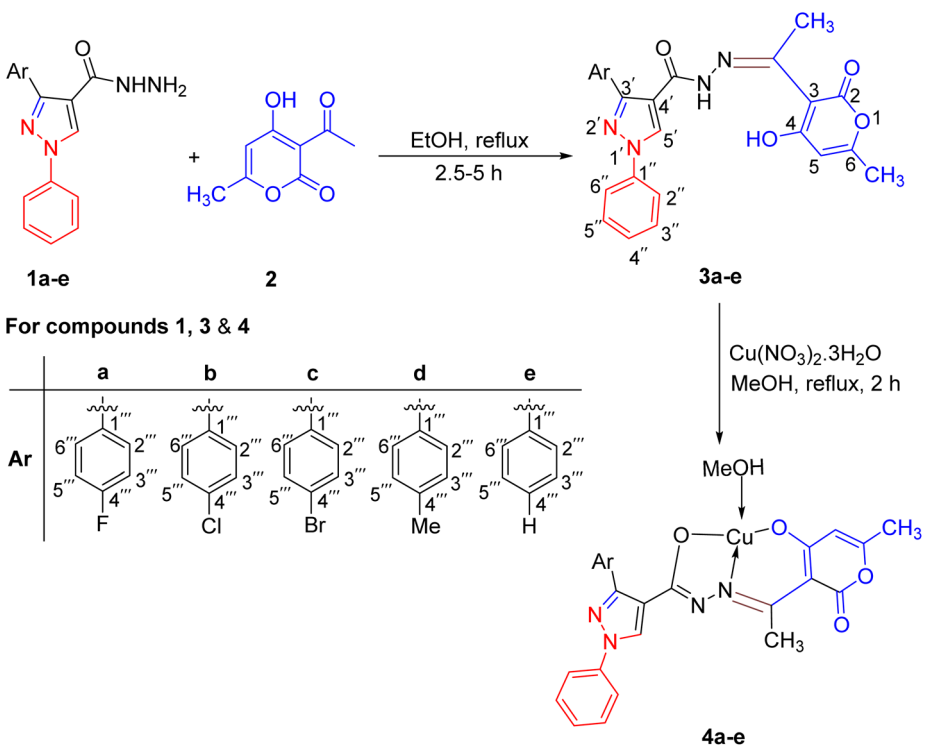

Scheme 2 Preparation of ligands (3a–e) and their copper(II) complexes (4a–e).

© 2025 The Author(s). Published by the Royal Society of Chemistry

Open Access Article. Published on 03 November 2025. Downloaded on 2/11/2026 12:55:24 AM. This article is licensed under a Creative Commons Attribution-NonCommercial 3.0 Unported Licence.

509 and 479–474 cm^{-1}, respectively, further confirms complexes' formation in which pyrazole ligands are linked with copper(II) ions through the oxygen-atom of the carbonyl group, the nitrogen-atom of the CH_3–C=N– group and oxygen-atom of the solvent (MeOH) molecules.[26] The results of FT-IR spectroscopy are in agreement with UV-vis spectral data, further validating the complex formation.

2.2.3 NMR spectroscopy. In the ^{1}H NMR spectrum of **3e** (an exemplary candidate), the appearance of proton signals near δ 9.14 ppm and 5.90 ppm due to pyrazole-5′-*H* and DHA moiety 5-H, respectively, supports the formation of Schiff's bases. For aryl protons, a multiplet was detected around δ 7.41 to 7.96 ppm. Two doublets were also found in the spectrum of the Schiff's base due to *p*-substitution on the Ph-ring linked to the 3rd carbon of the pyrazole ring. In the ^{13}C NMR spectrum, chemical shift values (δ) at around 181 ppm, 169 ppm, and 163 ppm indicated the presence of two carbonyl groups and azomethine moiety (C=N) in compound **3e**. In ^{1}H NMR spectra, signals appearing near δ 2.14 and 2.63 ppm are due to methyl protons of azomethine and DHA moieties, respectively. One additional singlet at 3.36 ppm for the methyl group was also observed in the case of compound **3d**. The ligands also have D_2O exchangeable singlets that appeared at 11.47 ppm and 16.22 ppm as an outcome of the –NH and –OH groups, respectively.

2.2.4 Mass spectrometry. In mass spectra, the resulting peaks of molecular ions were correlated with the molecular weights of the prepared compounds to ensure their formation. Well-defined molecular ion peaks at *m*/*z* values 447.14, 463.11, 507.06, 443.18, and 429.16 appeared due to **3a–e**, respectively, which coincide with the formula weights of the Schiff's bases. Whereas **4a–e** metal complexes exhibited *m*/*z* 540.0594, 557.9914, 602.05, 537.3055, and 523.9485 molecular ion peaks as a result of $[M^+ + H]$ ions, respectively, corresponding to their molecular masses and thus confirm the complexation of the ligands with copper(II) ions in a 1 : 1 ratio.

2.2.5 Thermogravimetric analysis (TGA). TGA findings disclosed the thermally stable character and presence of water/solvent molecules within or outside the coordination sphere, which were examined in a range of 25–1000 °C. The thermogram of complex **4b**, depicted in the SI, exhibits three consecutive weight loss phases, consistent with the proposed formulae,[27] rather than abrupt weight loss. The initial phase demonstrates a 6% weight reduction attributable to the disintegration of MeOH molecules at temperatures ranging from 52 to 65 °C. Meanwhile, the second and third decomposition phases exhibit weight losses of 21.77% (1.9640 mg) and 38.34% in the temperature ranges of 220–240 °C and 240–800 °C, respectively, as a consequence of the ligand moiety breaking down, leaving Cu(II) oxide as residue.[28a] Therefore, the complex went through three phases of decomposition described above,

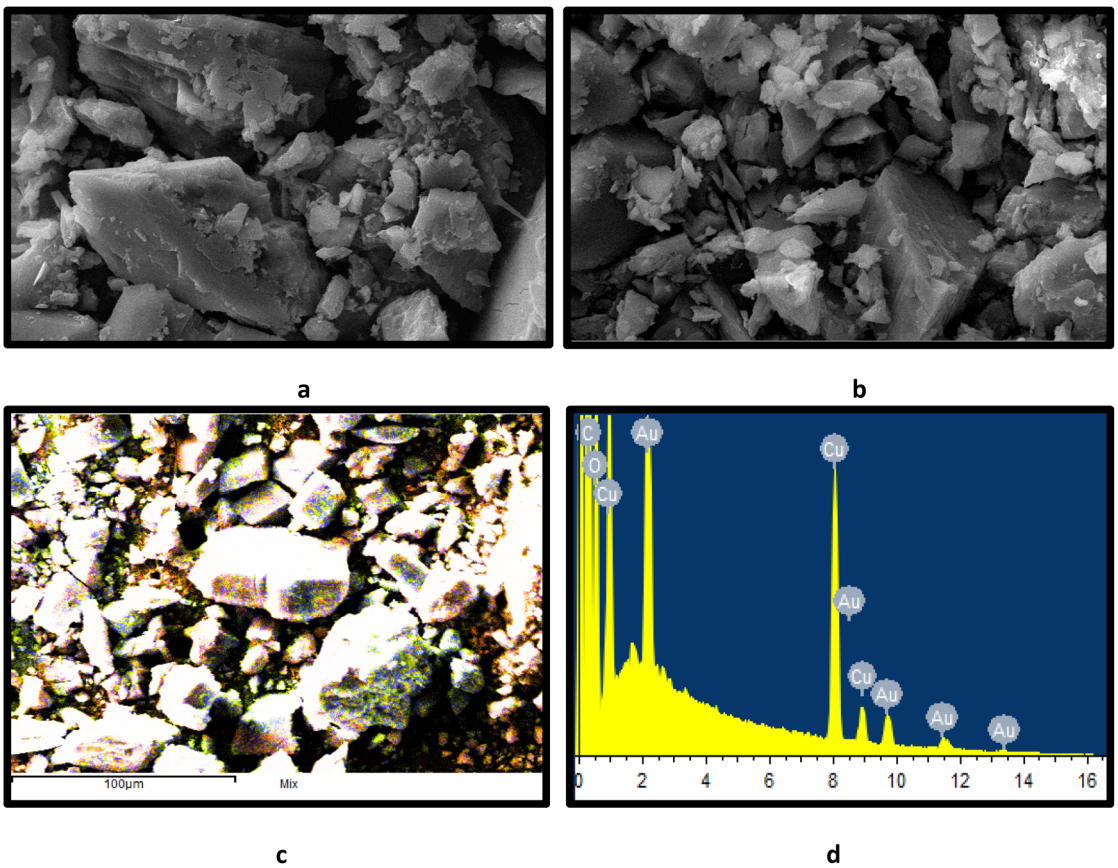

Fig. 3 SEM images of complex **4e** (a and b), elemental mapping (c) and EDX spectrum (d).

Open Access Article. Published on 03 November 2025. Downloaded on 2/11/2026 12:55:24 AM.
This article is licensed under a Creative Commons Attribution-NonCommercial 3.0 Unported Licence.

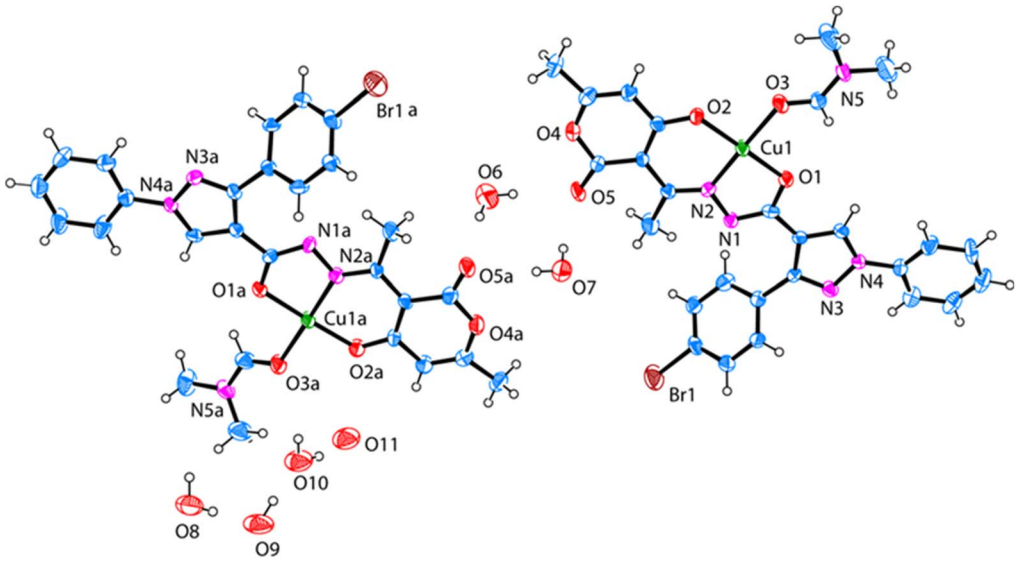

Fig. 4 ORTEP diagram of copper complex-**4c** with thermal ellipsoids set to 40% probability level.

leaving a metal oxide residue. Consequently, the results demonstrated the stable feature of the complexes up to 220 °C, as well as the presence of solvent molecules (MeOH) within the coordination sphere and the non-volatile nature of the complexes.

2.2.6 Electron spin resonance (ESR) spectroscopy. The ESR spectroscopy is a valuable tool for demonstrating the magnetic properties of the metal complexes. The spectra of Cu(II) complexes are presented in Fig. 12 (SI). The g_{avg} values of the copper complexes were observed at a 2.26 > 2.0023 trend, and the unpaired electrons existed in all complexes.[28b] It is suggested that in complexes, copper ion is present in the +2 oxidation state and has one unpaired electron.

2.2.7 Scanning electron microscopy-energy dispersive X-ray spectroscopy (SEM-EDX) analysis. The SEM technique was used to illustrate the compounds' surface appearance, and obtained results indicated that the complexes possess diverse surface morphologies.

The micrographs of complex **4e** are depicted in Fig. 3(a and b) and have rectangular bar-like morphology. The analysis of EDX data was used to know the composition of **4**, and the results thus obtained are presented in Fig. 3(c and d). The percentage of experimental atoms is found to be around the predicted (theoretical) values, in line with the results. The complex's micrograph in Fig. 3d revealed several key components, including C, N, and O elements. The presence of Cu(II) metal in the complex's micrograph validated the complex's formation.[29a] Elemental mapping (Fig. 3c) reflects an even distribution of copper ions. Thus, results obtained from EDX further support the ligand–metal ion complexation. SEM-EDX spectra of all complexes **4a–e** are given in the (Fig. 13–17).

2.2.8 Single-crystal X-ray diffraction study of copper(II) complex 4c. To confirm the geometry, stoichiometry, and binding sites of the ligands with copper ions, crystals of copper complex **4c** were obtained by recrystallizing the complex in a mixture of DMF and MeOH, involving the slow evaporation of

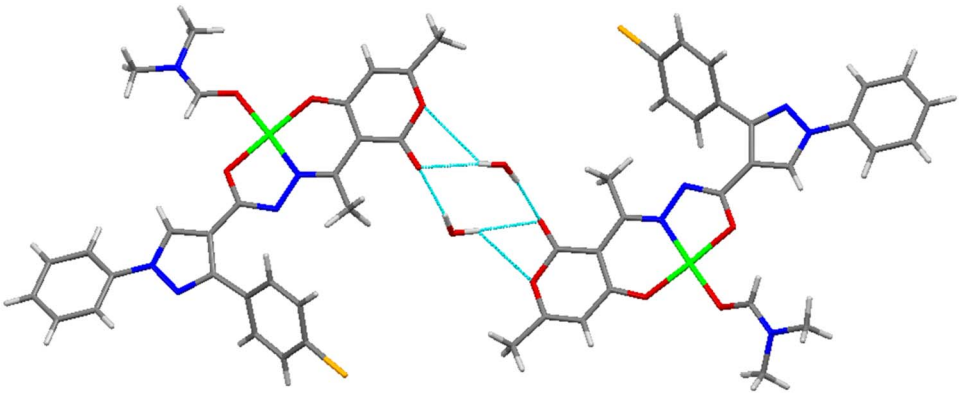

Fig. 5 A lattice diagram of copper complex **4c** is presented along the a and b planes, highlighting the intermolecular hydrogen bonding interactions between the molecules.

© 2025 The Author(s). Published by the Royal Society of Chemistry

Open Access Article. Published on 03 November 2025. Downloaded on 2/11/2026 12:55:24 AM.
This article is licensed under a Creative Commons Attribution-NonCommercial 3.0 Unported Licence.

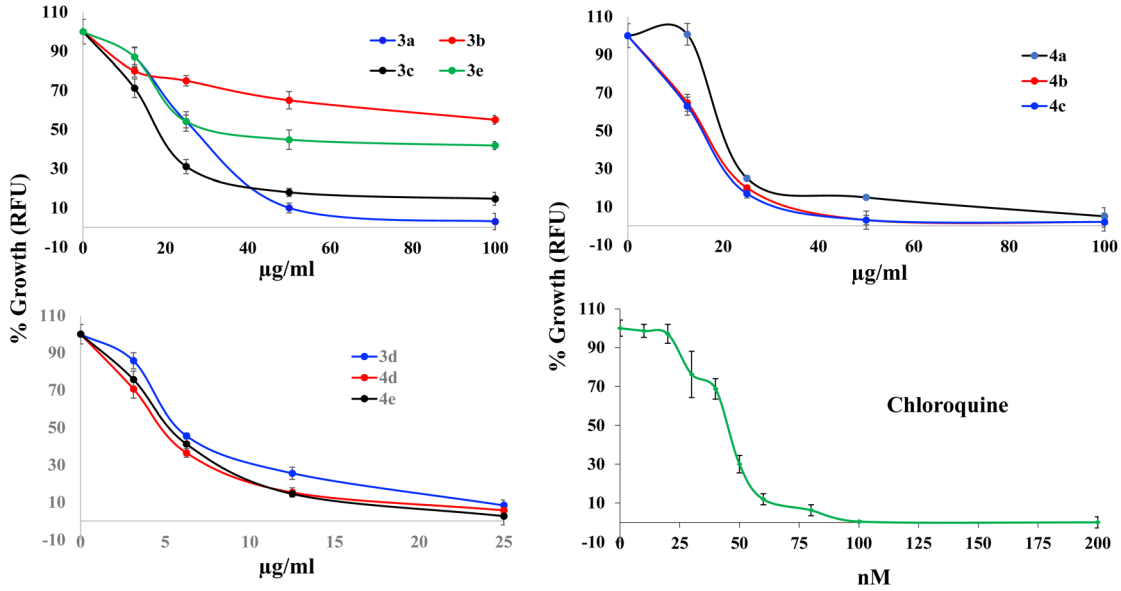

Fig. 6 Growth inhibition curve and parasitemia of Pf3D7 post 72 h of treatments with all ligands (**3a–e**) and their complexes (**4a–e**).

the solvent. A good-sized single crystal of **4c** was carefully selected for analyzing its structure *via* the X-ray diffraction technique at room temperature.

The complex with the *P*-1 space group crystallized in the triclinic system. The copper centre has a square planar geometrical arrangement of doubly deprotonated L^{2-} ligand coordinated with copper(II) metal ion (Fig. 5).

This coordination involves the deprotonation of hydroxyl (OH) group of the pyranone ring, the azomethine nitrogen, the amide carboxyl (C=O) oxygen, and oxygen atom of DMF solvent molecule. The Cu1–N_2 (imino) bond length is 1.906 Å, Cu1–O2 is 1.885 Å, and Cu1–O1 is 1.903 Å, which are in close agreement with the reported values.[29b] In comparison, the Cu1–O3 (DMF) bond is slightly lengthier at 1.968 Å. The tridentate ligand adopts a coplanar conformation, illustrating significant electron delocalization. The complex also shows weak hydrogen bonding involving a water molecule and the carbonyl O5 and O4 atoms of the pyrone ring. Detailed crystallographic refinement data, including key bond angles and lengths, are presented in Table S3 (SI), offering a comprehensive structural description of copper complex-**4c**.

2.3 Biological evaluation

2.3.1 Antimalarial activity. To demonstrate the versatility of the synthesized compounds (Scheme 2), Schiff's bases **3a–e** and their copper(II) complexes (**4a–e**) were screened for assessing their antimalarial potential against *Plasmodium falciparum* (Pf3D7). All samples were used at doses of 12.5 µg mL^{-1} in preliminary experiments using Chloroquine as a reference drug. It was observed that all candidates inhibited the parasite's growth in a concentration-dependent manner (Fig. 18, SI and Fig. 6).

Compounds **3d**, **4d** & **4e** displayed the highest antimalarial potential against the *P. falciparum* with IC_{50} values of 5.2, 4.8 & 5.2 µM (Table S4, SI), and the RBC hemolytic study also revealed that complexes **4d** & **4e** (Fig. 27 and 28, SI) suppressed 100% parasitemia at a concentration of 12.5 µg mL^{-1}. In comparison, complex **4a** suppressed 100% parasitemia at 100 µg mL^{-1}. In contrast, compounds **3a**, **3d**, **4c**, and **4b** suppressed approximately 98% at 100 µg mL^{-1} (Table 1). All investigated compounds, except **3b**, **4a** and **4c**, exhibited excellent selectivity towards Pf3D7 parasitemia, ranging from 2.08 to 18.38. Compound **3d** exhibited the highest selectivity index (SI = 18.38), followed by **3e** (SI = 9.48) and **4d** (SI = 6.02).

It was noted that the substitution at the *p*-position of the aryl ring linked to the position-3 of the pyrazole nucleus is showing variation in antimalarial potential. Among ligands, **3a** & **3d** demonstrated the highest % of suppression (*i.e.*, 97%) at higher concentration (100 µg mL^{-1}) against *P. falciparum*. Interestingly, copper(II) complexes **4a–e** were more active even at low

Table 1 *In vitro* antimalarial activity of the compounds against *P. falciparum* (Pf3D7) after 72 h

	% Parasitemia		% Suppression	
Compounds	12.5 µg mL^{-1}	100 µg mL^{-1}	12.5 µg mL^{-1}	100 µg mL^{-1}
3a	93.33	**2.95**	6.67	**97.05**
3b	68.38	62.57	31.62	37.43
3c	52.90	5.81	47.10	**94.19**
3d	42.19	**2.47**	57.81	**97.53**
3e	73.81	37.62	26.19	62.38
4a	**2.0**	**0.0**	**98.0**	**100.0**
4b	21.71	**1.90**	78.29	**98.10**
4c	23.62	**1.90**	78.29	**98.10**
4d	**0.0**	**0.0**	**100.0**	**100.0**
4e	**0.0**	**0.0**	**100.0**	**100.0**
CQ	**0.95**	**0.95**	**99.05**	**99.05**

Open Access Article. Published on 03 November 2025. Downloaded on 2/11/2026 12:55:24 AM. This article is licensed under a Creative Commons Attribution-NonCommercial 3.0 Unported Licence.

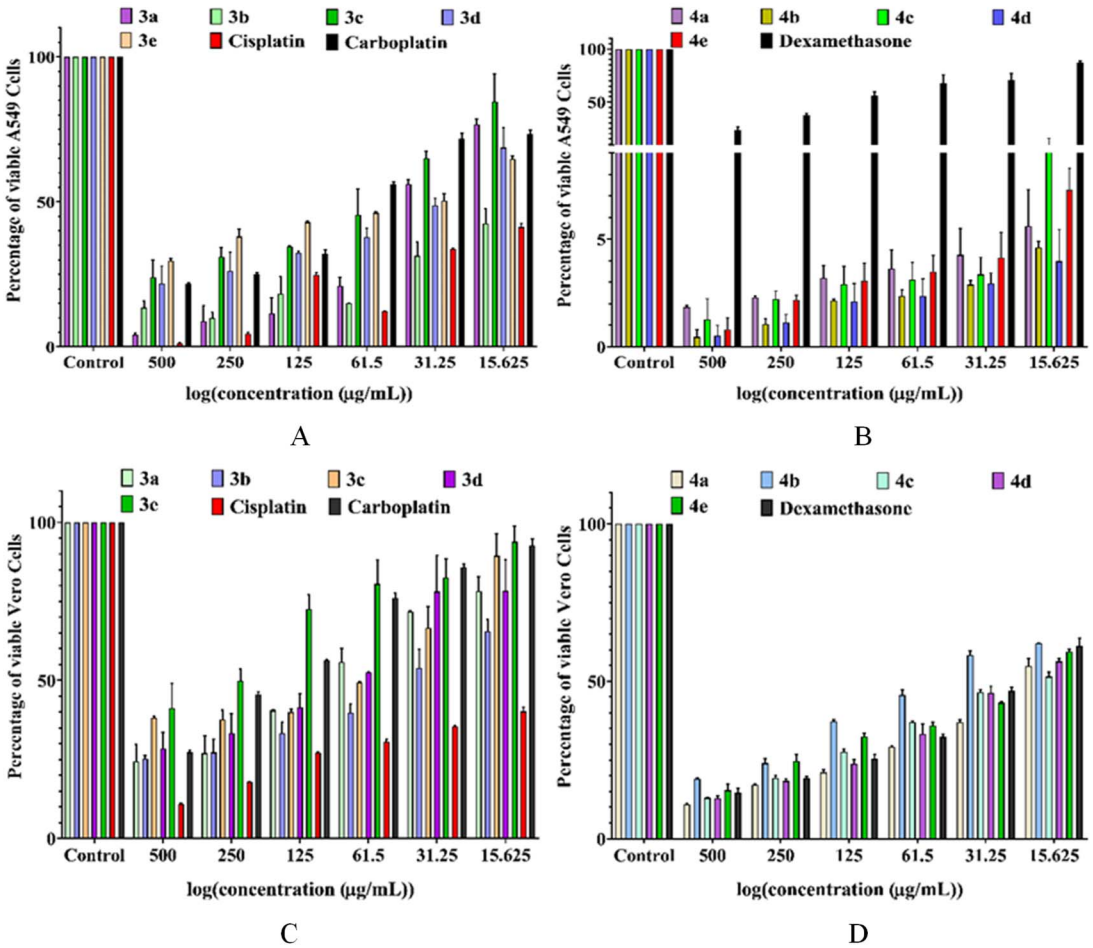

Fig. 7 Viability percentage of A549 cells; (A) **3a–e**, cisplatin and carboplatin; (B) **4a–e** and dexamethasone; and vero cells; (C) **3a–e**, cisplatin and carboplatin; (D) **4a–e** and dexamethasone on treating at different concentrations of screened compounds.

concentration against *P. falciparum* as compared to ligands (Fig. 6).

2.3.2 Anticancer activity. All synthesized compounds have been administered for their *in vitro* antiproliferative potential against two different cell lines: Vero (African green monkey kidney cells) and A549 (Human lung adenocarcinoma cells), using DMSO (0.25%) as a negative control. Cytotoxicity of compounds was assessed in a concentration-dependent manner starting from 500 μg mL^{-1} for 48 h. Clinically approved standard drugs, Carboplatin, Cisplatin and Dexamethasone were used as positive controls.

All of the examined compounds expressed excellent anticancer potential in a dose-dependent manner with a minimum inhibitory concentration (IC_{50}) under 100 μg mL^{-1} (Fig. 7). Among **3a–e**, compound **3b** demonstrated the most potent antiproliferative activity with an IC_{50} of 31.17 ± 6.4 μM, followed by **3a** (IC_{50} = 68.48 ± 2.4 μM) and **3d** (IC_{50} = 97.03 ± 4.5 μM).

Compound **3e**, with a slightly higher IC_{50} (145.52 ± 12.37 μM), demonstrated the highest selectivity index (SI = 4.56), followed by **3b** (SI = 3.25) and **3a** (SI = 2.78). All the examined compounds, except **3c** and **3d**, depicted higher selectivity towards A549 cells in the range of 2.78 to 13.48 as compared to the reference drugs, carboplatin (SI = 2.57), cisplatin (SI = 1.35) and dexamethasone (SI = 0.23).

Notably, copper complexes **4a–e** exhibited excellent anticancer potential with higher selectivity towards A549 cells, outperforming **3a–e** and the reference drugs. Among them, **4c** and **4b** depicted remarkable anticancer potential against A549 cells with IC_{50} values of 7.06 ± 0.8 and 6.9 ± 0.0 μM, respectively, followed by **4d** (7.10 ± 0.2 μM), **4a** (7.40 ± 0.3 μM) and **4e** (7.81 ± 0.0 μM). Further, **4b** showed the highest selectivity (SI > 13) towards A549 cells, surpassing all the reference drugs with minimum cytotoxicity towards Vero cells. Furthermore, **4d** and **4e** exhibit almost comparable selectivity, with values of 7.58 and 7.60, respectively, followed by **4c** (SI = 7.06) and **4a** (SI = 5.70), indicating them as favourable candidates for further studies (Table S5, SI).

Overall, copper(II) complexes **4a–e** exhibited enhanced cytotoxicity and high selectivity as compared to the ligand **3a–e** and standard drugs. The structure–activity study (SAR) suggested that substitution at position-4 of the aryl ring linked to position-3 of the pyrazole moiety significantly increases anticancer activity. In the case of aryl substitution at the third position of the pyrazole nucleus in **4a–e**, the trend observed for anticancer

 © 2025 The Author(s). Published by the Royal Society of Chemistry

Open Access Article. Published on 03 November 2025. Downloaded on 2/11/2026 12:55:24 AM. This article is licensed under a Creative Commons Attribution-NonCommercial 3.0 Unported Licence.

potential was as follows: F < Br < Me < Cl. Furthermore, copper complexation plays a crucial role and leads to increased anticancer efficacy in the case of **4a–e** compared to its counterpart **3a–e**. Therefore, results indicate that **4a–e** and **3e** may be considered as suitable candidates for further target exploration that may be established as new anticancer entities in the future.

2.3.3 Antimicrobial activity. The antimicrobial capacity of compounds has been assessed against a fungal strain, *C. albicans*, and two bacteria, *E. coli* and *B. subtilis*. After screening the antimicrobial ability of the compounds, we further evaluated the MIC values using a broth microdilution assay.[30] MIC can be defined as the minimum amount of compound that can inhibit cell growth by 50%.[30] In this study, Schiff base ligands were found to be more active against the bacterial strains than their corresponding copper(II) complexes, except **4e**. In case of *B. subtilis* and *E. coli*, compound **4e** established the most intriguing antibacterial capabilities, with MIC values of 0.02 and 0.07 mg mL^{-1}, respectively. However, Table S6 (SI) points out that none of the tested compounds were found efficacious against *C. albicans*.

2.3.4 Structure–activity relationship (SAR). The conclusion drawn from the evaluation of antimalarial, anticancer, and antimicrobial activity is based on the presumption regarding the structure–activity relationship (SAR).

The order of antimalarial potential was observed as: *p*-methylphenyl > phenyl > *p*-bromophenyl > *p*-chlorophenyl > *p*-fluorophenyl. It seems that the inductive effect has a significant influence on antimalarial activities, as +I effect leads to increased and −I effect decreases the antimalarial activity as per IC_{50} values. However, the antimalarial potential was diminished in the case of a *p*-chlorophenyl substituent, as analyzed by the concentration-dependent suppression of parasitemia at 100 μg mL^{-1}.

The observed order of anticancer ability among **3a–e** is: *p*-chlorophenyl > *p*-fluorophenyl > *p*-methylphenyl > *p*-bromophenyl. Substitution at position-4 of the aryl ring attached to position-3 of the pyrazole nucleus substantially affects the anticancer activity. Among the ligands, the compound **3e** exhibited an excellent level of anticancer potential. However, the Cu(II) complex **4b**, having a *p*-chlorophenyl substituent at the *para*-location of the phenyl group, displayed the highest selectivity (SI > 13) towards A549 cells.

Furthermore, the bioactivity studies concluded that the copper(II) complexes are found to be more efficient bioactive agents than the ligands owing to a variety of features, including DNA cleavage, chelation, lipophilicity, charge distribution, and binding ability. On the other side, the trend is reversed in antimicrobial activity, where the ligand performs better than its corresponding Cu(II) complexes, except for the methyl-substituted Cu(II) complex, which displayed better activity than its ligand.

3. Computational study of compounds

The optimized geometries of the ligands **3a–e** and their copper complexes **4a–e** are shown in Fig. 30 (SI). We have also analyzed frontier molecular orbitals (FMOs) to understand the stability and reactivity patterns of ligands and their copper complexes.

From the energy gap of the FMOs of ligands, it is concluded that **3d** is the most reactive among ligands, while **3e** is the most stable (Fig. 29, SI). Similarly, for the copper(II) complexes, there is not much difference in energy gaps. Still, these complexes show a smaller energy gap than the corresponding ligands (Fig. 8). The compounds' docking scores are noteworthy *in silico* binding affinities for DHFR-TS wild-type mutant structures. Additionally, the most active compounds expressed higher docking scores towards the DHFR-TS mutant structure. It suggested that the most potent compounds have a specific affinity for the mutant DHFR-TS complexes, and it could be a potential pathway for malaria resistance. The best docked poses of compounds **3a**, **3d**, **4b**, and **4e** are shown in Fig. 8, and the rest are given in the SI (Fig. 31–36).

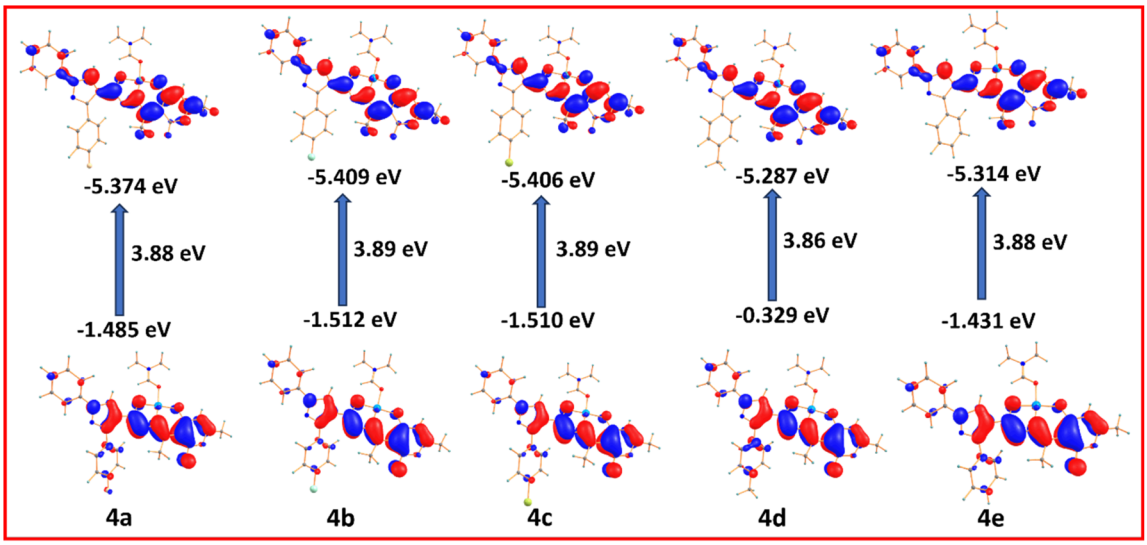

Fig. 8 Frontier molecular orbitals of complexes **4a–e** and energy differences.

Open Access Article. Published on 03 November 2025. Downloaded on 2/11/2026 12:55:24 AM. This article is licensed under a Creative Commons Attribution-NonCommercial 3.0 Unported Licence.

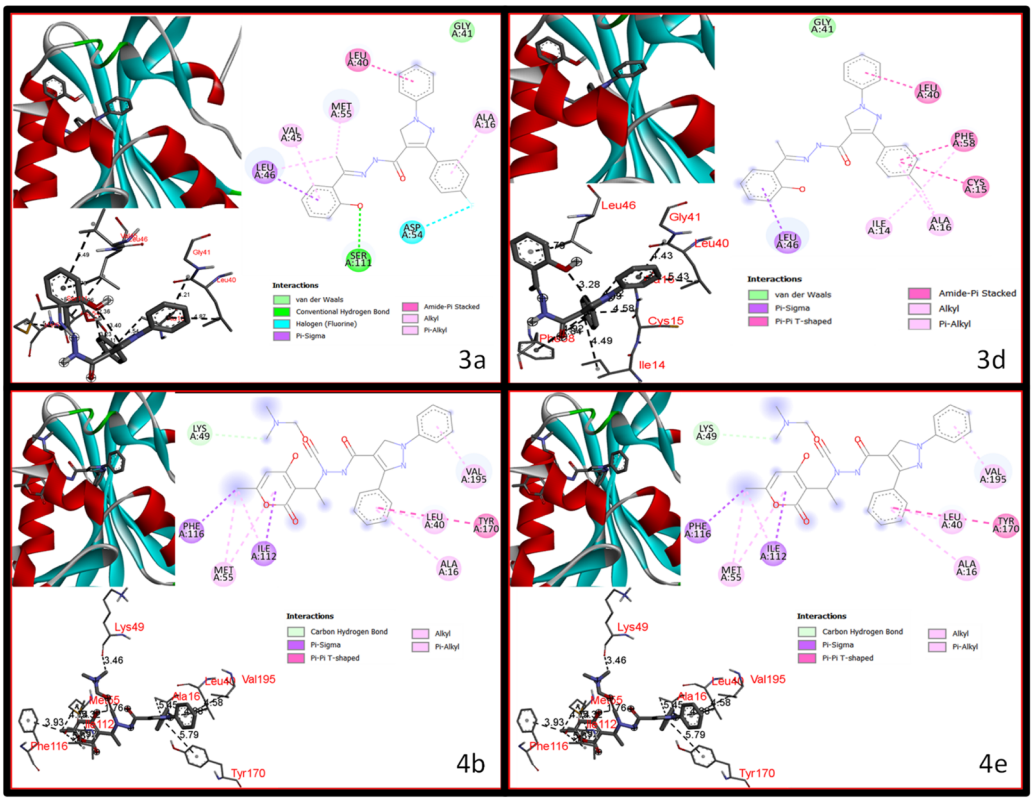

Fig. 9 3D and 2D plots of the interactions between the compounds **3a**, **3d**, **4b**, and **4e** with the active places of the wild-type mutant-pf DHFR-TS (PDB ID: 1j3i).

The docked poses' highest negative binding energy values show the highest binding affinity. As observed in Fig. 9, the docking pose of **3a** demonstrates advantageous interactions with the coordinating site of the wild-type pf DHFR-TS. The compound **3a** is involved in H-bonding with the amino acid SER111 at a distance of 2.36 Å and halogen interaction with ASP54 at a distance of 3.23 Å. Other interactions, such as van der Waals, π-alkyl, π-sigma, and amide-π-stacked, are also present. The different binding energies obtained from the outcome of molecular modelling of all compounds are depicted in Table S7 (SI). Similarly, hydrogen, alkyl, pi-alkyl, pi-sigma, pi-sulphur, and pi–pi bonds are found to be dominant in the binding interactions of the examined ligands **3a–e** and their complexes **4a–e** with protein.

Docking experiments revealed that the amino acids that contributed to the interactions with the compounds are ILE112, SER111, ALA16, PHE58, VAL45, LEU46, PRO113, CYS15, GLY41, ASP54, YR170 MET55. The values of binding energy achieved from the results of docking analysis of **3a–e** with the highest binding affinity are −10.4, −10.5, −10.4, −10.6, and −10.4 kcal mol^{-1}, respectively.

Similarly, for the complexes **4a–e**, the calculated binding energy values with the highest binding affinity are −10.7, −10.1, −10.4, −10.2, and −11.1, respectively. The dominant interactions present in **4a–e** are H-bonding, pi-alkyl, pi-sulphur, and pi-sigma. A species with the highest binding potential will have the most negative binding energy value. These negative values of binding energies indicate a higher binding potential for proteins. Compound **4e** (Table S7, SI) exhibited the highest negative value of binding affinity, which may suggest its higher efficiency in binding to the protein.

A crucial role played by hydrogen bonding and pi-sulfur in linking compounds to proteins has been identified. Theoretical outcomes suggested that all compounds (**3a–e**, **4a–e**) have excellent binding affinity for wild-type pf DHFR-TS, which is also correlated with *in vitro* antimalarial results. Moreover, noteworthy interactions with the protein were also observed in the case of docking analysis of **4e.** The results of the docking analysis supported the concept that complex formation with Cu(II) ion is vital to show excellent antimalarial activity. Based on the results of binding affinity, the overall order of studied molecules is **4e** > **4a** > **3d** > **3b** > **4c** = **3a** = **3c** = **3e** > **4d** > **4b**.

4. Experimental

4.1 Materials

The chemicals and reagents, including Dehydroacetic acid(>99%), Acetophenone (>99%), *p*-fluoroacetophenone, *p*-chloroacetophenone (>99%), *p*-bromoacetophenone (>99%), *p*-methylacetophenone (≥98%), copper(II) nitrate trihydrate (≥98%), were utilized as received from commercial suppliers without any further purification.

4.2 Instrumentation

Fourier-Transform Infrared (FT-IR) spectra were recorded on a PerkinElmer BX III spectrophotometer using KBr pellets in the

© 2025 The Author(s). Published by the Royal Society of Chemistry

Open Access Article. Published on 03 November 2025. Downloaded on 2/11/2026 12:55:24 AM. This article is licensed under a Creative Commons Attribution-NonCommercial 3.0 Unported Licence.

4000–400 cm^{-1} range. The Schiff's base ligands' NMR spectral data were collected using the Bruker Avance III 500 MHz NMR instrument. The ESR spectral data of Cu(II) complexes were recorded using the JES-FA200 ESR spectrophotometer with an X-band, a standard (tetracyanoethylene), and a 3000 gauss magnetic field. Using alumina as the reference, the PerkinElmer Diamond apparatus was used to evaluate the compounds' thermal data in a pure argon gas atmosphere. The melting points were measured on the hot-stage Gallenkamp device in open capillaries and are uncorrected. The mass spectral data were recorded on a SCIEX Triple TOF 5600 spectrometer in DMSO as a solvent. Using a PerkinElmer 750 UV-vis spectrophotometer, the spectra in a range of 200–800 nm wavelength were recorded by using a quartz cuvette with a 10 mm path length. Data collection was performed using the X-ray diffractometer (Rigaku Super-Nova) with Mo-Kα radiation (wavelength $\lambda = 0.71073$ nm) and a HyPix3000 CCD-detector (Fig. 4). The collected data were processed by using the software CrysAlisPro. The crystal structure was initially solved using Direct Methods in SIR2004[31a] and Olex2[31b] software, followed by refinement through Least Squares minimization in ShelXL.[31c]

4.3 General procedure

4.3.1 Synthesis of phenylhydrazones of differently substituted acetophenones (3′a–e)

4.3.1.1 Procedure. Acetophenone (**1′e**, 5 g, 0.04 mol) and phenylhydrazine (**2′**, 4.5 g, 0.04 mol) dissolved in ethanol separately were mixed in a round-bottom flask (RBF). Added 40 mL of ethanol, followed by two drops of concentrated solution. H_2SO_4 with the help of a capillary. Heated the reaction mixture to 35–40 °C on a magnetic stirrer with a hot plate, maintaining constant stirring for 25–45 min. The completion of the reaction was assessed by using thin-layer chromatography (TLC), using ethyl acetate: hexane (1 : 9) as a solvent system. A yellowish coloured solid was obtained after cooling. Filtered the solid and washed the resultant solid with chilled ethanol.

4.3.2 Synthesis of pyrazole-4-carbaldehydes (4′a–e)

4.3.2.1 Procedure. Synthesis of pyrazole-4-carbaldehydes (**4′a–e**) consists of two steps, in which the first step involves the preparation of the Vilsmeier–Haack reagent. Initially, DMF (5.2 g, 0.07 mol) was taken in a dried round-bottom flask (RBF). The RBF was then kept over an ice bath. Next, POCl3 (11.32 g, 0.07 mol) was added dropwise while maintaining a temperature of 0–5 °C. In the second step, a cold DMF (15 mL) was used to dissolve acetophenone phenylhydrazone **3′e** (5 g, 0.023 mol). After that, the reaction mixture was kept at 0–5 °C for 20 min. And then added Vilsmeier–Haack reagent in a dropwise manner. Stirred the reaction mixture for 4–5 h at 65–70 °C, and poured it into cold water (500 mL). Sodium bicarbonate was added to make the reaction mixture alkaline. The product thus obtained on vacuum filtration was washed thoroughly with water. Compounds **4′a–d** were also prepared by adopting a similar procedure (Scheme 1). Physical data of compounds **4′a–e** are presented in Table S1 (SI).

4.3.3 Synthesis of 1, 3-diphenyl-1*H*-pyrazole-4-carboxylic acids (5′a–e)

4.3.3.1 Procedure. 1, 3-Diphenyl-1*H*-pyrazole-4-carboxylic acids (**5′a–e**) were synthesized by the oxidation of 1, 3-diphenyl-1*H*-pyrazole-4-carbaldehydes (**4′a–e**) using $KMnO_4$ as an oxidizing agent. Initially, a 1 : 1 mixture of H_2O and *t*-BuOH was prepared, and to this mixture, 1,3-diphenyl-1*H*-pyrazole-4-carbaldehyde (**4′e**, 4 g, 0.016 mol) was added. Then, a solution of $KMnO_4$ (3 g, 0.019 mol) in H_2O was added dropwise over a period of 2.2 h while stirring at 70–75 °C. Then, 10% aq. KOH solution was used to make the solution alkaline, and the solution was then filtered. The resulting pH of the filtrate was adjusted to 2 by adding concentrated HCl. The solid thus obtained was filtered and washed properly using cold water. Dried the final product to obtain a white powder and noted the melting point. Physical data of compounds **5′a–e** are presented in Table S1 (SI).

4.3.4 Synthesis of esters (6′a–e)

4.3.4.1 Procedure. A methanolic solution of pyrazole-4-carboxylic acid (**5′e**, 3 g, 0.01 mol) was mixed with thionyl chloride (1.89 g, 0.015 mol) in a dropwise manner. The reaction mixture was refluxed for 5 h, and a white solid appeared on cooling. The solid product thus obtained was filtered, washed with methanol, and allowed to dry at ambient temperature. Noted the m.pt and yield of the product. Similarly, other derivatives **6′a–d** were prepared and characterization data are given in Table S1 (SI).

4.3.5 Synthesis of hydrazides (1a–e)

4.3.5.1 Procedure. An excess of hydrazine hydrate (1.68 g, 0.03 mol) was mixed with an ethanolic solution of ester (**6′e**, 1 g, 0.003 mol, 10 mL (ethanol) at room temperature, and the reaction mixture was stirred for 4 h. The excess solvent was then distilled out to yield the white precipitates. Filtered the solid thus obtained and dried at ambient temperature. Noted the m.pt and yield of the product. Similarly, other derivatives **1a–d** were prepared, and characterization data are given in Table S1 (SI).

4.3.6 Synthesis of Schiff's base ligands (3a–e)

4.3.6.1 Procedure. Dehydroacetic acid (**2**, 0.6 g, 3.5 mmol) was dissolved in 3 mL of ethanol and added dropwise to an ethanolic solution of 1,3-diphenyl-1*H*-pyrazole-4-carbohydrazides (**1e**, 1 g, 3.5 mmol) under constant stirring. The resultant mixture was then refluxed at 85 °C for 2.5 h. The white precipitates obtained after completion of the reaction were filtered, washed with ethanol, and dried at room temperature. Noted the m.pt and yield of the product **3e**. Similarly, other derivatives **3a–d** were prepared.

4.3.7 Physical and spectroscopic data of the compounds 3a–e

4.3.7.1 (Z)-3-(4-fluorophenyl)-N′-(1-(4-hydroxy-6-methyl-2-oxo-2H-pyran-3-yl)ethylidene)-1-phenyl-1H-pyrazole-4-carbohydrazide (3a). Colour: off white; yield: 1.08 g, 72%; observed melting point: 185–188 °C; FT-IR (KBr, υ_{max}, cm^{-1}): 3145 (O–H Str.), 3069 (N–H Str.), 1699 (C=O Str.), 1648 (C=O_{DHA} Str.), 1593 (C=N Str.); UV-Vis (DMSO), λ_{max}: 270 nm ($\pi \rightarrow \pi^*$), 370 nm ($n \rightarrow \pi^*$); ^{1}H-NMR (400 MH_Z; DMSO-d_6, δ_H): 2.14 (s, 3H, CH_3–C=N), 2.64 (s, 3H, 6-CH_3), 5.81 (s, 1H, 5-H), 7.28–7.32 (m, 2H, 3‴ & 5‴-H), 7.41–7.44 (m, 1H, 4″-H), 7.58–7.61 (m, 2H, 3″ & 5″-H), 7.92–7.96 (m, 4H, 2‴ & 6‴-H, 2″ & 6″-H), 9.14 (s, 1H, 5′-H), 11.47 (s, 1H, NH, D_2O exchangeable), 16.19 (s, 1H, OH D_2O exchangeable);

Open Access Article. Published on 03 November 2025. Downloaded on 2/11/2026 12:55:24 AM. This article is licensed under a Creative Commons Attribution-NonCommercial 3.0 Unported Licence.

MS (EI) M^+ (*m*/*z*) calcd. for $C_{24}H_{19}FN_4O_4$: 446.13, found: 447.14 (M^++H).

*4.3.7.2 (Z)-3-(4-chlorophenyl)-N′-(1-(4-hydroxy-6-methyl-2-oxo-2H-pyran-3-yl)ethylidene)-1-phenyl-1H-pyrazole-4-carbohydrazide (**3b**).* Colour: off white; yield: 0.95 g, 64%; observed melting point: 215–218 °C; FT-IR (KBr, υ_{max}, cm^{-1}): 3178 (O–H Str.), 3072 (N–H Str.), 1699 (C=O Str.), 1647 (C=O Str.), 1574 (C=N Str.); UV-vis (DMSO), λ_{max}: 273 nm ($\pi \rightarrow \pi^*$), 369 nm ($n \rightarrow \pi^*$); ^{1}H-NMR (400 MH_Z; DMSO-d_6, δ_H): 2.15 (s, 3H, CH_3–C=N), 2.66 (s, 3H, 6-CH_3), 5.91 (s, 1H, 5-H), 7.43–7.46 (m, 1H, 4″-H), 7.54–7.56 (m, 2H, 3‴ & 5‴-H), 7.59–7.63 (m, 2H, 3″ & 5″-H), 7.93–7.97 (m, 4H, 2‴ & 6‴-H, 2″ & 6″-H), 9.17 (s, 1H, 5′-H), 11.47 (s, 1H, NH, D_2O exchangeable), 16.23 (s, 1H, OH, D_2O exchangeable); MS (EI) M^+ (*m*/*z*) calcd. for $C_{24}H_{19}ClN_4O_4$: 462.10, Found: 463.11/464.11 [M^++H]/[M^++2] (3 : 1).

*4.3.7.3 (Z)-3-(4-bromophenyl)-N′-(1-(4-hydroxy-6-methyl-2-oxo-2H-pyran-3-yl)ethylidene)-1-phenyl-1H-pyrazole-4-carbohydrazide (**3c**).* Colour: off white; yield: 0.97 g, 68%; observed melting point: 185–190 °C; FT-IR (KBr, υ_{max}, cm^{-1}): 3145 (O–H Str.), 3069 (N–H Str.), 1699 (C=O Str.), 1648 (C=O Str.), 1593 (C=N Str.); UV-vis (DMSO), λ_{max}: 282 nm ($\pi \rightarrow \pi^*$), 376 nm ($n \rightarrow \pi^*$); ^{1}H-NMR (400 MH_Z; DMSO-d_6, δ_H): 2.16 (s, 3H, CH_3–C=N), 2.67 (s, 3H, 6-CH_3), 5.93 (s, 1H, 5-H), 7.44–7.47 (m, 1H, 4″-H), 7.55–7.71 (m, 4H, 3‴ & 5‴-H, 3″ & 5″-H), 7.87–7.98 (m, 4H, 2‴ & 6‴-H, 2″ & 6″-H), 9.18 (s, 1H, 5′-H), 11.52 (s, 1H, NH, D_2O exchangeable), 16.24 (s, 1H, OH, D_2O exchangeable); MS (EI) M^+ (*m*/*z*) calcd. for $C_{24}H_{19}BrN_4O_4$: 506.05, found: 507.06/508.06 [M^+]/[M^++2] (1 : 1).

*4.3.7.4 (Z)-3-(4-methylphenyl)-N′-(1-(4-hydroxy-6-methyl-2-oxo-2H-pyran-3-yl)ethylidene)-1-phenyl-1H-pyrazole-4-carbohydrazide (**3d**).* Colour: off white; yield: 1 g, 67%; observed melting point: 193–197 °C; FT-IR (KBr, υ_{max}, cm^{-1}): 3150 (O–H Str.), 3070 (N–H Str.), 1701 (C=O Str.), 1648 (C=O_{DHA} Str.), 1589 (C=N Str.); UV-vis (DMSO), λ_{max}: 279 nm ($\pi \rightarrow \pi^*$), 343 nm ($n \rightarrow \pi^*$); ^{1}H-NMR (400 MH_Z; DMSO-d_6, δ_H): 2.14 (s, 3H, CH_3–C=N), 2.36 (s, 3H, 4‴-CH_3), 2.64 (s, 3H, 6-CH_3), 5.89 (s, 1H, 5-H), 7.26–8.04 (m, 9H, Ar–H), 9.19 (s, 1H, 5′-H), 11.48 (s, 1H, NH, D_2O exchangeable), 16.20 (s, 1H, OH, D_2O exchangeable); MS (EI) M^+ (*m*/*z*) calcd. for $C_{25}H_{22}N_4O_4$: 442.46, found: 443.18 [M^++H].

*4.3.7.5 (Z)-N′-(1-(4-hydroxy-6-methyl-2-oxo-2H-pyran-3-yl)ethylidene)-1,3-diphenyl-1H-pyrazole-4-carbohydrazide (**3e**).* Colour: off white; yield: 1.3 g, 85%; observed melting point: 190–193 °C; FT-IR (KBr, υ_{max}, cm^{-1}): 3106 (O–H Str.), 2957 (N–H Str.), 1670 (C=O Str.), 1541 (C=O_{DHA} Str.), 1467 (C=N Str.); UV-vis (DMSO), λ_{max}: 278 nm ($\pi \rightarrow \pi^*$), 348 nm ($n \rightarrow \pi^*$); ^{1}H-NMR (400 MH_Z; DMSO-d_6, δ_H): 2.14 (s, 3H, CH_3–C=N), 2.63 (s, 3H, 6-CH_3), 5.90 (s, 1H, 5-H), 7.41–7.49 (m, 4H, 3‴ & 5‴-H, 3″ & 5″-H), 7.58–7.61 (m, 2H, 4‴-H & 4″-H), 7.86–7.88 (d, 2H, 2‴ & 6‴-H), 7.95–7.96 (d, 2H, 2″ & 6″-H), 9.14 (s, 1H, 5′-H), 11.47 (s, 1H, NH, D_2O exchangeable), 16.22 (s, 1H, OH, D_2O exchangeable); MS (EI) M^+ (*m*/*z*) calcd. for $C_{24}H_{20}N_4O_4$: 428.44, found: 429.16 [M^++H].

4.3.8 Synthesis of Cu(II) complexes (4a–e)

4.3.8.1 Procedure. A heated methanolic solution of ligand (**3e**, 0.5 g, 1.1 mmol) was added in a dropwise manner to another mixture containing methanol and $[Cu(NO_3)_2]\cdot 3H_2O$ (0.3 g, 1.1 mmol) while continuously stirring at 450 rpm. The reaction mixture was then heated to reflux for 2 h and further stirred for another 12 h at room temperature at 450 rpm. The resulting green precipitates were filtered and washed properly with methanol and then dried at room temperature. Noted the m.pt and yield of the product. Similarly, other copper(II) complexes **4a–d** were prepared.

4.3.9 Physical and spectroscopic data of the compounds 4a–e

*4.3.9.1 Cu(II) complex (**4a**).* Colour: green; yield: 0.49 g, 82%; observed melting point: 220–225 °C; FT-IR: (KBr, υ_{max}, cm^{-1}): 1687 (C=O Str.), 1588 (C=N Str.), 1526 (C=N Str.), 479 (M–N Str.), 549 (M–O Str.); UV-vis (DMSO), λ_{max}: 264 nm ($\pi \rightarrow \pi^*$), 362 nm ($n \rightarrow \pi^*$), 447 nm ($^2B_{1\,g} \rightarrow {}^2E_{1\,g}$), 559 nm ($^2B_{1\,g} \rightarrow {}^2A_{1\,g}$); HRMS M^+ (*m*/*z*) calcd. for $C_{25}H_{21}CuFN_4O_5$: 539.0792, found: 540.0559.14 [M^++H].

*4.3.9.2 Cu(II) complex (**4b**).* Colour: green; yield: 0.5 g, 84%; observed melting point: 225°C-229 °C; FT-IR: (KBr, υ_{max}, cm^{-1}): 1677 (C=O Str.), 1592 (C=N Str.), 1541 (C=N Str.), 474 (M–N Str.), 560 (M–O Str.); UV-vis (DMSO), λ_{max}: 264 nm ($\pi \rightarrow \pi^*$), 363 nm ($n \rightarrow \pi^*$), 449 nm ($^2B_{1\,g} \rightarrow {}^2E_{1\,g}$), 559 nm ($^2B_{1\,g} \rightarrow {}^2A_{1\,g}$); HRMS M^+ (*m*/*z*) calcd. for $C_{25}H_{21}CuClN_4O_5$: 555.0496, found: 557.9914 [M^++2].

*4.3.9.3 Cu(II) complex (**4c**).* Colour: green; yield: 0.52 g, 88%; observed melting point: 220–224 °C; FT-IR: (KBr, υ_{max}, cm^{-1}): 1677 (C=O Str.), 1591 (C=N Str.), 1541 (C=N Str.), 479 (M–N Str.), 549 (M–O Str.), UV-vis (DMSO), λ_{max}: 264 nm ($\pi \rightarrow \pi^*$), 362 nm ($n \rightarrow \pi^*$), 447 nm ($^2B_{1\,g} \rightarrow {}^2E_{1\,g}$), 558 nm ($^2B_{1\,g} \rightarrow {}^2A_{1\,g}$); HRMS M^+ (*m*/*z*) calcd. for $C_{25}H_{21}CuBrN_4O_5$: 598.9991, found: 602.1348.

*4.3.9.4 Cu(II) complex (**4d**).* Colour: green; yield: 0.52 g, 87%; observed melting point: 230–235 °C; FT-IR: (KBr, υ_{max}, cm^{-1}): 1699 (C=O Str.), 1586 (C=N Str.), 1550 (C=N Str.), 478 (M–N Str.), 549 (M–O Str.); UV-vis (DMSO), λ_{max}: 264 nm ($\pi \rightarrow \pi^*$), 365 nm ($n \rightarrow \pi^*$), 451 nm ($^2B_{1\,g} \rightarrow {}^2E_{1\,g}$), 550 nm ($^2B_{1\,g} \rightarrow {}^2A_{1\,g}$); HRMS M^+ (*m*/*z*) calcd. for $C_{26}H_{24}CuN_4O_5$: 535.1043, found: 536.0594 [M^++H].

*4.3.9.5 Cu(II) complex (**4e**).* Colour: green; yield: 0.51 g, 85%; observed melting point: 229°C-233 °C; FT-IR: (KBr, υ_{max}, cm^{-1}): 1702 (C=O Str.), 1583 (C=N Str.), 1548 (C=N Str.), 474 (M–N Str.), 509 (M–O Str.); UV-vis (DMSO), λ_{max}: 264 nm ($\pi \rightarrow \pi^*$), 364 nm ($n \rightarrow \pi^*$), 559 nm ($^2B_{1\,g} \rightarrow {}^2A_{1\,g}$), HRMS M^+ (*m*/*z*) calcd. for $C_{25}H_{22}CuN_4O_5$: 521.0886, found: 523.9971[M^++2].

4.4 Computational studies

4.4.1 Density functional theory (DFT) and molecular docking studies. All the compounds were optimized at the DFT/B3LYP/6-311G(d,p) level[32,33] of theory in Gaussian16 software.[34] The optimized geometries of the ligands (**3a–e**) and their copper complexes (**4a–e**) are shown in Fig. 30 (SI). Furthermore, we have also analyzed frontier molecular orbitals (FMOs) to understand the stability and reactivity patterns of the ligands and their corresponding copper complexes under investigation. Molecular docking is used for identifying and developing drug candidates and is a computational technique for examining the biological activity of complexes at the molecular level.[35–38] We

 © 2025 The Author(s). Published by the Royal Society of Chemistry

Open Access Article. Published on 03 November 2025. Downloaded on 2/11/2026 12:55:24 AM. This article is licensed under a Creative Commons Attribution-NonCommercial 3.0 Unported Licence.

investigated the binding mechanisms of ligands (**3a–e**) and complexes (**4a–e**) in the active site for the wild-type mutant pf DHFR-TS (Plasmodium falciparum dihydrofolate reductase-thymidylate synthase) (PDB ID: 1j3i) as a potential antimalarial target for our compounds in an attempt to understand the observed pattern of *in vitro* antimalarial activity.[39] The interaction analysis between the pf DHFR-TS and the compounds (**3a–e** and **4a–e**) was conducted by using the AutoDock Vina program and AutoDock-Tools (ADT).[40] All water molecules surrounding the protein were removed before starting the docking calculation. When assigning grid box sizes ($40 \times 40 \times 40$ Å, centered at $X = 28.741985$, $Y = 5.926629$, $Z = 60.148934$), the residues associated with each protein's active site were taken into account, as guided by a previous study.[17,41,42] The ligand–protein interactions and the docked poses were visualized by using the tool Biovia Discovery Studio Visualizer 2021.[43]

4.5 Biological activity

4.5.1 Antimalarial activity

4.5.1.1 Cultivation of Plasmodium falciparum(Pf). Using the approach of Trager and Jensen[44] with slight modifications, a strain of Pf that was sensitive to Chloroquine (CQ, Sigma) (3D7) was kept in continuous culture. Parasite was obtained from Malaria Research and Reference Reagent Resource Center (MR4). The cultures were safeguarded in fresh group O^{+ve} human erythrocytes, which have been suspended at 4% haematocrit in the complete medium 16.2 g L^{-1} RPMI 1640 comprising 25 mM HEPES, 11.11 mM glucose (Gibco), 0.2% sodium bicarbonate (Sigma), 0.5% albumax I (Gibco), 45 g L^{-1} hypoxanthine (Sigma), and 50 g L^{-1} gentamicin (Gibco). The cultures were then incubated at 37 °C in a gaseous mixture of 5% oxygen, 5% carbon dioxide, and 90% nitrogen gas. To spread the culture, the spent medium was swapped out daily for a new, whole medium. Blood smears stained with Giemsa were studied under a microscope to track parasitemia. After 5% sorbitol treatment, a synchronized ring-stage parasite was produced.[44,45]

4.5.1.2 Assay for antiplasmodial activity. CQ (Positive control) stock solution was prepared in Milli-Q water. To obtain the needed drug concentrations, culture media were used to dilute each stock solution. 96-Well flat-bottom tissue culture plates were filled with solutions of CQ and compounds **3a–e** & **4a–e**. As previously mentioned,[46] the SYBR green I(Invitrogen) based fluorescent assay was employed for compounds (**3a–e**, **4a–e**) screening. Under typical culture conditions, sorbitol (Sigma)-synchronized ring-stage parasites (haematocrit: 2%, parasitemia: 1%) were cultured with or without increasing concentrations of compounds **3a–e** and **4a–e** in water. Each well was filled with Triton X-100 (0.08% v/v, Sigma), gently mixed twice using a multi-channel pipette, and then incubated for 1 h at 37 °C in the dark. A Victor fluorescence multi-well plate reader (PerkinElmer) with excitation and emission wavelengths centred at 485 and 530 nm, respectively, was used to plot the fluorescence counts against the compounds' concentration after subtracting the fluorescence counts for chloroquine from the counts observed in each well. The IC_{50} value was calculated by analyzing dose–response curves.

4.5.1.3 Hemolysis assay. After three spin washes in Phosphate Buffer Saline (PBS) at 1600 rpm for five min., fresh RBCs were re-suspended in PBS with a 2% haematocrit. RBCs were procured from Rotary Blood Bank, New Delhi. In 96-well plates, aliquots of a 100 µl solution were introduced to wells that contained varying concentrations of compounds **3a–e** and **4a–e**. The controls were PBS only (for baseline values) and 0.4% Triton X-100 in PBS (for 100% haemolysis). The samples (**3a–e** and **4a–e**) were centrifuged after 3 h of incubation at 37 °C, and the haemolytic activity was assessed using the supernatant, which A415 tracked. Control samples treated with Triton were diluted 10 times before absorbance was measured. Every data point had the baseline value (PBS control) subtracted. To express haemolysis as a percentage, a positive control (RBCs treated with Triton X-100) was given a 100% haemolysis value.

4.5.2 Cytotoxicity study

4.5.2.1 Cell culture. Human lung adenocarcinoma cells (A549 cells, non-small cell lung cancer cell line) and Vero cells (African green monkey kidney cells, non-cancerous, immortalized kidney epithelial cells) were conserved in Dulbecco's Modified Eagle Medium (DMEM). Both the cell lines were obtained from the National Centre for Cell Science (NCCS), Pune, India. A 10% foetal bovine serum supplement (FBS: Gibco) was added to the culture media and Pen-Strep.[46] Cultures were continuously maintained in 5% CO_2 at 37 °C with constant humidity.

4.5.2.2 Cell viability assay. Using a yellow colored, 3-(4,5-dimethylthiazole-2-yl)-2,5-biphenyl tetrazolium bromide salt and an MTT test, cell viability was examined. At 75% to 80% confluency during trypsinization, cells were collected by using 0.25% trypsin–EDTA. They counted the cells using a hemocytometer. After seeding 96-well plates with 1×10^4 cells/well, the plates were cultured in a CO_2 incubator for 24 h.[47] The 96-well plate culture was incubated for 48 h after test compounds (**3a–e**) with different concentrations of serial dilutions (500 µg mL^{-1} maximum concentration) were added after 24 h. The highest concentrations for compounds **4a–e** and Dexamethasone, Cisplatin, and Carboplatin were 50 µg mL^{-1}. Dexamethasone, Cisplatin, and Carboplatin were standard antiproliferative drugs. DMSO was used as a solvent for the compounds at a final concentration of 0.05%.

4.5.2.3 MTT assay. After 48 h of incubation, the viability of the cell culture treated with the test substances was evaluated. For the removal of the compounds, 96-well culture plates were gently cleaned with 1X phosphate buffer saline (PBS). 96-Well plates were filled with MTT salt solution (5 mg mL^{-1} in 1X PBS), resulting in a final conc. of 0.5 mg mL^{-1} in each well. The formazan crystal was solubilized with DMSO and incubated for 30 min. Following the 3 h incubation period. The absorbance of 96-well plates was then measured at 570 nm using a Synergy H1 microplate reader. All the experiments were performed in triplicate, and IC_{50} values were calculated for each test compound in GraphPad Prism 8.0.1 by fitting the experimental results into the sigmoidal equation.

Open Access Article. Published on 03 November 2025. Downloaded on 2/11/2026 12:55:24 AM. This article is licensed under a Creative Commons Attribution-NonCommercial 3.0 Unported Licence.

4.5.2.3.1 Selectivity index. The selectivity index (SI) for compounds with anticancer activity was calculated by dividing the IC_{50} concentrations of non-cancerous Vero cells by the IC_{50} concentration of A549 cells.

4.5.3 Antimicrobial activity

4.5.3.1 Microorganisms and culture. The present investigation used two bacterial strains, (*Bacillus subtilis* subsp. *Subtilis* JJBS250, *E. coli* DH5α) and a fungal culture (*Candida albicans*). Fungal culture was cultivated on potato dextrose agar,[48] whereas bacterial cultures were cultivated and maintained on LB agar.

4.5.3.2 Antibacterial assay. Lysogeny Broth (LB) was used to cultivate bacterial cultures overnight at 37 °C with stirring at 200 rpm. On Petri plates made of LB agar, bacterial cultures were disseminated after being combined with molten agar (0.8%). After 30 min., a sterile borer was used to create 10 mm wells in the Petri plates. Stock solutions of the compounds at 1 mg mL^{-1} and 5 mg mL^{-1} concentrations were introduced to wells. Ampicillin, an antibiotic, was used as a normative medication. After 24 h, the growth inhibition zone was measured. DMSO was employed as a negative control. The 50% inhibitory concentration (IC_{50}) of each compound was calculated using varying ligand and metal complex concentrations.

4.5.3.3 Antifungal assay. To obtain the spore suspension (1×10^6 spores/ml), a fungal culture was cultivated on Potato Dextrose Agar (PDA) slants for 72 h at 30 °C. On PDA Petri plates, the spore suspension from the fungal culture was combined with melted agar (0.8% agar).[47] A sterile borer was used to create wells (10 mm) in the Petri plates after they had been left for 30 min. The organic compounds' stock solutions at 1 mg mL^{-1} and 5 mg mL^{-1} concentrations were prepared in DMSO and put into wells. The standard drug, Fluconazole was served as a positive control. As a control, DMSO was also employed. The 50% inhibitory concentration (IC_{50}) of each compound was calculated using varying ligand and metal complex concentrations.

5. Conclusion

In the present study, five pyrazole-based Schiff's base ligands and their copper(II) complexes were prepared. Spectroscopic and physical analysis provided a comprehensive characterization of the synthesized compounds (**3a–e**, **4a–e**). Thermogravimetric measurement confirmed that the complexes are thermally stable up to 220 °C. The results of a single-crystal X-ray diffraction study of complex **4c** revealed that the complexes possess a square planar geometry.

The complexes were found to be remarkably more effective than the Schiff base ligands in biological screening, following the trend **4b** > **4e** > **4d** > **4c** > **4a** in terms of anticancer activity. From the antimalarial results, it is concluded that compounds **3a** and **3d** exhibited significant antimalarial activity against *Plasmodium falciparum* with 97% of suppression of parasitemia while complexes **4a**, **4d**, and **4e** exhibited excellent inhibitory activity surpassing the efficacy (100% suppression) of the reference drug (99%). Furthermore, molecular docking results revealed that Cu(II) complexes have enhanced binding affinity towards wild-type mutant *P. falciparum* (pf DHFR-TS) compared to their uncoordinated ligands.

Among all compounds, **4b** showed excellent antiproliferative ability with an IC_{50} value of 3.84 ± 0.1 μM and a selectivity index of 13.48 towards cancer cells. Compounds **4c**, **4d** & **5e** also displayed promising anticancer ability with an SI greater than 7, suggesting them as suitable candidates for further detailed screening studies. Compound **4d** exhibited the strongest antimalarial and anticancer properties among all compounds, with significant IC_{50} values of 4.8 and 3.81 ± 0.1 μg mL^{-1}, respectively. Compound **4e** was an effective antibacterial agent against *B. subtilis* with an MIC of 0.02 mg mL^{-1}.

SAR data further revealed that pharmacological efficacy in copper(II) complexes is found to be higher than that of their corresponding ligands. Overall, it is concluded that copper(II) complexes have great potential to be developed as new bioactive agents in the future with excellent selectivity towards lung cancer cells. Therefore, by offering an antimalarial and anticancer medication that provides fresh perspectives on medicinal chemistry for *in vivo* research, this study explained the practical and theoretical significance of Schiff's base ligands and their copper(II) complexes.

Author contributions

Pratima Kumari: writing-original draft review and editing, methodology, and investigation. Aman Kumar: writing-original draft preparation. Ramesh Kataria: writing-review & editing, data curation, formal analysis, supervision and resources. Naveen Kumar Kaushik: writing-review & editing, antimicrobial and antimalarial analysis. Mukhtar Ahmed: DFT analysis and software investigation. Azaj Ansari: DFT analysis and software investigation. Ekta: writing-original draft preparation and analysis. Mettle Brahma: anticancer analysis, validation. Mulaka Maruthi: anticancer analysis, validation. Yangala Sudheer Babu: anticancer analysis, validation. Bijender Singhr: writing-review & editing, antimicrobial and antimalarial analysis. Vinod Kumar: writing-review & editing, resources, conceptualization, supervision.

Conflicts of interest

The authors declared that there is no conflict of interest.

Data availability

CCDC 2424331 contain the supplementary crystallographic data for this paper.[49]

Data details have been given in the supplementary information (SI) uploaded with the manuscript. Supplementary information is available. See DOI: https://doi.org/10.1039/d5ra06008g.

Acknowledgements

The authors thank Central University of Haryana, Panjab University, Chandigarh, and Amity Institute of Virology and

 © 2025 The Author(s). Published by the Royal Society of Chemistry

Open Access Article. Published on 03 November 2025. Downloaded on 2/11/2026 12:55:24 AM. This article is licensed under a Creative Commons Attribution-NonCommercial 3.0 Unported Licence.

Immunology, Amity University, Uttar Pradesh for providing laboratory facilities. The authors also thank DST Government of India for the DST-FIST II grant for establishing the single crystal facility at the Department of Chemistry, Panjab University, Chandigarh. The Central University of Haryana is also acknowledged for providing financial assistance to Ms Pratima Kumari. Mr. Aman Kumar is grateful to the Haryana State Council for Science & Technology (HSCST), Haryana (File No.: HSCSIT/21) and the Council of Scientific and Industrial Research (CSIR), New Delhi (File No.: 09/1152(16491)/2023-EMR-I) for providing financial assistance.

References

1 *Cisplatin, Chemistry and Biochemistry of a Heading Anticancer Drug*, ed. B. Hippert, Wiley-VCH, Weinheim, 1999.
2 T. Boulikas and M. Vougiouka, *Oncol. Rep.*, 2023, **10**, 1663–1682.
3 K. Singh, Y. Kumar, P. Puri, C. Sharma and K. R. Aneja, *Arabian J. Chem.*, 2017, **10**, S978–S987.
4 M. Wehbe, A. W. Leung, M. J. Abrams, C. Orvig and M. B. Bally, *Dalton Trans.*, 2017, **46**, 10758–10773.
5 (*a*) T. Wang and Z. Gu, *Curr. Med. Chem.*, 2006, **13**, 525–537; (*b*) F. Tisato, C. Marzano, M. Porchia, M. Pellei and C. Santini, *Med. Res. Rev.*, 2010, **30**, 708–749; (*c*) A. Hordyjewska, L. Popiołek and J. Kocot, *BioMetals*, 2014, **27**, 611–621; (*d*) A. De Luca, A. Barile, M. Arciello and L. Rossi, *J. Trace Elem. Med. Biol.*, 2019, **55**, 204–213.
6 P. Kumari, M. Choudhary, A. Kumar, P. Yadav, B. Singh, R. Kataria and V. Kumar, *Inorg. Chem. Commun.*, 2023, **158**, 111409.
7 (*a*) D. Denoyer, S. Masaldan, S. L. Fontaine and M. A. Cater, *Metallomics*, 2015, **7**, 1459–1476; (*b*) S. Tardito, I. Bassanetti, C. Bignardi, L. Elviri, M. Tegoni, C. Mucchino, O. Bussolati, R. F. Gazzola and L. Marchiò, *J. Am. Chem. Soc.*, 2011, **133**, 6235–6242; (*c*) J. Zuo, C. Bi, Y. Fan, D. Buac, C. Nardon, K. G. Daniel and Q. P. Dou, *J. Inorg. Biochem.*, 2013, **118**, 83–93; (*d*) C. H. Ng, S. M. Kong, Y. L. Tiong, M. J. Maah, N. Sukram, M. Ahmad and A. S. B. Khoo, *Metallomics*, 2014, **6**, 892–906; (*e*) S. Zehra, T. Roisnel and F. Arjmand, *ACS Omega*, 2019, **4**, 7691–7705.
8 A. Boora, J. Devi, T. Rom and A. K. Paul, *J. Mol. Struct.*, 2023, **1284**, 135386.
9 N. Nayak, J. Ramprasad and U. Dalimba, *Bioorg. Med. Chem. Lett.*, 2015, **25**, 5540–5545.
10 Y. R. Li, C. Li, J. C. Liu, M. Guo, T. Y. Zhang, L. P. Sun, C. J. Zheng and H. R. Piao, *Bioorg. Med. Chem. Lett.*, 2015, **25**, 5052–5057.
11 F. J. Meng, T. Sun, W. Z. Dong, M. H. Li and Z. Z. Tuo, *Arch. Pharm.*, 2016, **349**, 168–174.
12 H. Chuang, L. C. S. Huang, M. Kapoor, Y. J. Liao, C. L. Yang, C. C. Chang, C. Y. Wu, J. R. Hwu, T. J. Huang and M. H. Hsu, *MedChemComm*, 2016, **7**, 832–836.
13 H. N. Hafez, A. R. B. A. El-Gazzar and S. A. Al-Hussain, *Bioorg. Med. Chem. Lett.*, 2016, **26**, 2428–2433.
14 J. B. Shi, W. J. Tang, X. B. qi, R. Li and X. H. Liu, *Eur. J. Med. Chem.*, 2015, **90**, 889–896.
15 S. Viveka, P. Shama, S. Naveen, N. K. Lokanath and G. K. Nagaraja, *RSC Adv.*, 2015, **5**, 94786–94795.
16 Y. N. Mabkhot, N. A. Kaal, S. Alterary, S. S. Al-Showiman, A. Barakat, H. A. Ghabbour and W. Frey, *Molecules*, 2015, **20**, 8712–8729.
17 A. A. Bekhit, A. M. Hassan, H. A. A. El Razik, M. M. El-Miligy, E. J. El Agroudy and A. E. D. A. Bekhit, *Eur. J. Med. Chem.*, 2015, **94**, 30–44.
18 K. Karrouchi, S. Radi, Y. Ramli, J. Taoufik, Y. N. Mabkhot, F. A. Al-aizari and M. Ansar, *Molecules*, 2018, **23**, 134–218.
19 N. Raghav and M. Singh, *Bioorg. Chem.*, 2017, **75**, 38–49.
20 (*a*) A. Abiko, J. C Roberts, T. Takemasa and S. Masamune, *Tetrahedron Lett.*, 1986, **27**, 4537–4540; (*b*) N. H. Amin, M. I. A. Hamed, M. M. Abdel-Fattah, A. H. A. Abusabaa and M. T. El-Saadi, *Bioorg. Chem.*, 2021, **116**, 105394.
21 B. D. Hosangadi and R. H. Dave, *Tetrahedron Lett.*, 1996, **37**, 6375–6378.
22 V. A. Chornous, M. K. Bratenko, M. V. Vovk and I. I. Sidorchuk, *Pharm. Chem. J.*, 2001, **35**, 26–28.
23 N. K. Richa, S. Negi, A. Kumar, E. Zangrando, R. Kataria and V. Saini, *Dalton Trans.*, 2021, **50**, 13699–13711.
24 (*a*) X. Liu, H. Feng, Y. Li, X. Ma, F. Chen and Q. Yan, *J. Ind. Eng. Chem.*, 2022, **115**, 193–208; (*b*) A. A. El-Bindary, M. G. El-Desouky and M. A. M. El-Afify, *Biointerface Res. Appl. Chem.*, 2022, **12**, 1053–1075.
25 R. Fekri, M. Salehi, A. Asadi and M. Kubicki, *Inorg. Chim. Acta*, 2019, **484**, 245–254.
26 J. Devi, S. Sharma, S. Kumar, B. Kumar, D. Kumar, D. K. Jindal and S. Das, *Appl. Organomet. Chem.*, 2022, **36**, e6760.
27 M. Yadav, S. Sharma and J. Devi, *J. Chem. Sci.*, 2021, **133**, 1–22.
28 (*a*) S. S. Kumar, S. Biju and V. Sadasivan, *J. Mol. Struct.*, 2018, **1156**, 201–209; (*b*) S. S. Ali Fathima, M. M. S. Meeran and E. R. Nagarajan, *Struct. Chem.*, 2020, **31**, 521–539.
29 (*a*) R. P. Bakale, N. Naik, S. S. Machakanur, C. V. Mangannavar, I. S. Muchchandi and K. B. Gudasi, *J. Mol. Struct.*, 2018, **1154**, 92–99; (*b*) Y. L. Tunde, D. O. Segun, Z. Sizwe, M. K. Hezekiel, A. L. Isiaka, M. L. Monsurat and M. Nonhlangabezo, *ACS Omega*, 2021, **6**, 13704–13718.
30 N. Kumari, S. Singh, V. Kumari, S. Kumar, V. Kumar and A. Kumar, Ouabain potentiates the antimicrobial activity of aminoglycosides against *Staphylococcus aureus*, *BMC Complementary Altern. Med.*, 2019, **19**, 1–12.
31 (*a*) M. C. Burla, R. Caliandro, M. Camalli, B. Carrozzini, G. L. Cascarano, C. Giacovazzo, M. Mallamo, A. Mazzone, G. Polidori and R. Spagna, *J. Appl. Crystallogr.*, 2012, **45**, 357–361; (*b*) O. V. Dolomanov, L. J. Bourhis, R. J. Gildea, J. A. K. Howard and H. Puschmann, *J. Appl. Crystallogr.*, 2009, **42**, 339–341; (*c*) G. M. Sheldrick, *Acta Crystallogr., Sect. C:Struct. Chem.*, 2015, **71**, 3–8.
32 (*a*) A. D. Becke, *J. Chem. Phys.*, 1992, **96**, 2155–2160; (*b*) M. A. Arafath, F. Adam, M. B. K. Ahamed, M. R. Karim, M. N. Uddin, B. M. Yamin and A. Abdou, *J. Mol. Struct.*, 2023, **1278**, 134887.

Open Access Article. Published on 03 November 2025. Downloaded on 2/11/2026 12:55:24 AM.
This article is licensed under a Creative Commons Attribution-NonCommercial 3.0 Unported Licence.

33 E. Papajak, J. Zheng, X. Xu, H. R. Leverentz and D. G. Truhlar, *J. Chem. Theory Comput.*, 2011, **7**, 3027–3034.
34 M. J. Frisch, G. W. Trucks, H. B. Schlegel, G. E. Scuseria, M. A. Robb, J. R. Cheeseman Jr. J. A. Montgomery, T. Vreven, K. N. Kudin, J. C. Burant, J. M. Millam, S. S. Iyengar, J. Tomasi, V. Barone, B. Mennucci, M. Cossi, G. Scalmani, N. Rega, G. A. Petersson, H. Nakatsuji, M. Hada, M. Ehara, K. Toyota, R. Fukuda, J. Hasegawa, M. Ishida, T. Nakajima, Y. Honda, O. Kitao, H. Nakai, M. Klene, X. Li, J. E. Knox, H. P. Hratchian,J. B. Cross, V. Bakken, C. Adamo, J. Jaramillo, R. Gomperts, R. E. Stratmann, O. Yazyev, A. J. Austin, R. Cammi, C. Pomelli, J. W. Ochterski, P. Y. Ayala, K. Morokuma, G. A. Voth, P. Salvador, J. J. Dannenberg, V. G. Zakrzewski, S. Dapprich, A. D. Daniels, M. C. Strain, O. Farkas, D. K. Malick, A. D. Rabuck, K. Raghavachari, J. B. Foresman, J. V. Ortiz, Q. Cui, A. G. Baboul, S. Clifford, J. Cioslowski, B. B. Stefanov, G. Liu, A. Liashenko, P. Piskorz, I. Komaromi,R. L. Martin, D. J. Fox, T. Keith, M. A. Al-Laham, C. Y. Peng, A. Nanayakkara, M. Challacombe, P. M. W. Gill, B. Johnson, W. Chen, M. W. Wong, C. Gonzalez, and J. A. Pople, *Gaussian 16, Revision A.03*, Gaussian, Inc., Wallingford CT, 2016.
35 M. Azam, S. R. Barik, P. K. Mohapatra, M. Kumar, A. Ansari, R. K. Mohapatra, A. T. Kruszynska and S. I. Al-Resayes, *Russ. J. Inorg. Chem.*, 2023, **19**, 1–8.
36 R. Sahu, R. K. Mohapatra, S. I. Al-Resayes, D. Das, P. K. Parhi, S. Rahman, L. Pintilie, M. Kumar, M. Azam and A. Ansari, *J. Saudi Chem. Soc.*, 2021, **25**, 101193.
37 M. Naqi Ahamad, M. Shahid, A. Ansari, M. Kumar, M. Ahmad, R. Arif, I. M. Khan and R. Uddin, *New J. Chem.*, 2019, **43**, 7511–7519.
38 R. K. Al-Shemary, R. K. Mohapatra, M. Kumar, A. K. Sarangi, M. Azam, H. S. Tuli, A. Ansari, P. K. Mohapatra and K. Dhama, *J. Mol. Struct.*, 2023, **1275**, 134676.
39 J. Yuvaniyama, P. Chitnumsub, S. Kamchonwongpaisan, J. Vanichtanankul, W. Sirawaraporn, P. Taylor, M. D. Walkinshaw and Y. Yuthavong, *Nat. Struct. Mol. Biol.*, 2003, **10**, 357–365.
40 O. Trott, A. J. Olson and A. Vina, *J. Comput. Chem.*, 2009, **31**, 455–461.
41 D. Kumar, S. I. Khan, B. L. Tekwani, P. Ponnan and D. S. Rawat, *Eur. J. Med. Chem.*, 2015, **89**, 490–502.
42 S. S. Maurya, S. I. Khan, A. Bahuguna, D. Kumar and D. S. Rawat, *Eur. J. Med. Chem.*, 2017, **129**, 175–185.
43 BIOVIA Systems, Dassault BIOVIA Discovery Studio, *Dassault Systems*, San Diego, 2021.
44 W. Trager and J. B. Jensen, *J. Sci.*, 2005, **91**, 484–486.
45 C. Lambros and J. P. Vanderberg, *J. Parasitol.*, 1979, **65**, 418–420.
46 M. Smilkstein, N. Sriwilaijaroen, J. X. Kelly, P. Wilairat and M. Riscoe, *Antimicrob. Agents Chemother.*, 2004, **48**, 1803–1806.
47 M. S. Altowyan, S. M Soliman, M. Haukka, N. H. Al-Shaalan, A. A. Alkharboush and A. Barakat, *ACS Omega*, 2022, **7**, 35743–35754.
48 Sapna and B. Singh, *Appl. Biochem. Biotechnol.*, 2014, **173**, 1885–1895.
49 CCDC 2424331: Experimental Crystal Structure Determination, 2025, DOI: **10.5517/ccdc.csd.cc2mcq7z**.

© 2025 The Author(s). Published by the Royal Society of Chemistry